

Spontaneous Chirality Flipping in an Orthogonal Spin-Charge Ordered Topological Magnet

H. Miao^{1,*†}, J. Bouaziz^{2,*‡}, G. Fabbri^{3,*}, W. R. Meier⁴, F. Z. Yang¹, H. X. Li^{1,5}, C. Nelson⁶, E. Vescovo⁶, S. Zhang⁷, A. D. Christianson¹, H. N. Lee¹, Y. Zhang^{8,9}, C. D. Batista^{8,10} and S. Blügel¹⁰

¹Materials Science and Technology Division, Oak Ridge National Laboratory, Oak Ridge, Tennessee 37831, USA

²Peter Grünberg Institut and Institute for Advanced Simulation, Forschungszentrum Jülich and JARA, D-52425 Jülich, Germany

³Advanced Photon Source, Argonne National Laboratory, Argonne, Illinois 60439, USA

⁴Department of Materials Science and Engineering, University of Tennessee, Knoxville, Tennessee, USA

⁵Advanced Materials Thrust, The Hong Kong University of Science and Technology (Guangzhou), Guangzhou, China

⁶National Synchrotron Light Source II, Brookhaven National Laboratory, Upton, New York 11973, USA

⁷Max-Planck-Institut für Physik komplexer Systeme, Nothnitzer Straße 38, 01187 Dresden, Germany

⁸Department of Physics and Astronomy, The University of Tennessee, Knoxville, Tennessee 37996, USA

⁹Min H. Kao Department of Electrical Engineering and Computer Science, University of Tennessee, Knoxville, Tennessee 37996, USA

¹⁰Quantum Condensed Matter Division and Shull-Wollan Center, Oak Ridge National Laboratory, Oak Ridge, Tennessee 37831, USA



(Received 4 December 2023; revised 24 January 2024; accepted 13 February 2024; published 21 March 2024)

The asymmetric distribution of chiral objects with opposite chirality is of great fundamental interest ranging from molecular biology to particle physics. In quantum materials, chiral states can build on inversion-symmetry-breaking lattice structures or emerge from spontaneous magnetic ordering induced by competing interactions. Although the handedness of a chiral state can be changed through external fields, a spontaneous chirality flipping has yet to be discovered. We present experimental evidence of chirality flipping via changing temperature in a topological magnet EuAl_4 , which features orthogonal spin density waves (SDW) and charge density waves (CDW). Using circular dichroism of Bragg peaks in the resonant magnetic x-ray scattering, we find that the chirality of the helical SDW flips through a first-order phase transition with modified SDW wavelength. Intriguingly, we observe that the CDW couples strongly with the SDW and displays a rare commensurate-to-incommensurate transition at the chirality flipping temperature. Combining with first-principles calculations and angle-resolved photoemission spectroscopy, our results support a Fermi surface origin of the helical SDW with intertwined spin, charge, and lattice degrees of freedom in EuAl_4 . Our results reveal an unprecedented spontaneous chirality flipping and lay the groundwork for a new functional manipulation of chirality through momentum-dependent spin-charge-lattice interactions.

DOI: [10.1103/PhysRevX.14.011053](https://doi.org/10.1103/PhysRevX.14.011053)

Subject Areas: Condensed Matter Physics, Magnetism

Chirality, a geometrical concept that distinguishes an object from its mirror image, has been proposed for over three decades as a potential mechanism for novel quantum states including spontaneous quantum Hall liquids [1], chiral spin liquids [2], and magnetic skyrmions [3,4].

Recently, chirality has experienced a revival in the context of correlated and geometrically frustrated electronic systems [5–12]. In these settings, chiral spin, charge, orbital, and pairing fields become strongly coupled, giving rise to intertwined orders [10] and long-range entangled quasiparticles [11,12]. In magnetic systems, the 1D and 2D chiral spin textures, as respectively shown in Figs. 1(b) and 1(c), have been widely observed in noncentrosymmetric lattices [13,14]. In these systems, the chirality or handedness, $\chi = \pm 1$, is usually transmitted to the spin system via the relativistic Dzyaloshinskii-Moriya (DM) interaction induced by spin-orbit coupling. Chiral spin orders can also spontaneously emerge in centrosymmetric materials [13–17], where competing magnetic interactions, such as the

*These authors are contributed equally to this work.

†Corresponding author: miaoh@ornl.gov

‡Corresponding author: j.bouaziz@fz-juelich.de

Published by the American Physical Society under the terms of the [Creative Commons Attribution 4.0 International license](https://creativecommons.org/licenses/by/4.0/). Further distribution of this work must maintain attribution to the author(s) and the published article's title, journal citation, and DOI.

Ruderman-Kittel-Kasuya-Yosida (RKKY), can yield equally populated $\chi = 1$ and -1 states. Experimentally, chirality manipulation has been achieved by applying external fields [13,18]. An outstanding question that remains is if the sign of chirality can be controlled by other means.

In this paper, we uncover an unprecedented spontaneous chirality flipping in EuAl_4 . EuAl_4 hosts nanometric skyrmions and the topological Hall effect under a magnetic field along the c axis [20–22]. At zero external magnetic field, EuAl_4 exhibits a tetragonal structure with $I4/mmm$ symmetry (centrosymmetric space group no. 139) at room temperature. Figure 1(d) summarizes the zero magnetic field symmetry breaking orders of EuAl_4 (see also Supplemental Material Fig. S1 and Table S1 [19]). Below $T_{\text{CDW}} = 140$ K, an incommensurate charge density wave (ICDW) develops along the crystalline c axis with $\mathbf{Q}_{\text{CDW}} = (0, 0, 0.183)$ in reciprocal lattice unit (r.l.u.). The \mathbf{Q}_{CDW} gradually shifts to the commensurate position at $(0, 0, 1/6)$ via decreasing temperature, which is typical for ICDW systems due to the lattice commensurate energy [23]. At $T_{\text{SDW}}^{(1)} = 15.4$ K, the system breaks the time-reversal symmetry \mathcal{T} by forming a double- \mathbf{Q} spin density wave (SDW) along the $[110]$ and $[1-10]$ directions. Below $T_{\text{SDW}}^{(2)} = 13.3$ K, the spin moment of the double- \mathbf{Q} SDW gains a finite c -axis component, leading to new interference magnetic peaks along

the $[100]$ and $[010]$ direction. The fourfold rotational symmetry C_4 in the ab plane is broken at $T_{\text{SDW}}^{(3)} = 12.3$ K, resulting in a stripe helical SDW [20,21]. Interestingly, although the helical SDW persists down to the lowest temperature at zero magnetic field, an additional first-order phase transition sets in at $T_\chi = 10.1$ K.

Here we use the circular dichroism (CD) of Bragg peaks in the resonant magnetic x-ray scattering (XRMS) to demonstrate that the first-order phase transition at T_χ leads to a spontaneous chirality flipping. CD XRMS is a direct experimental probe of chiral electronic orders [24–28]. Under the resonance condition, where the incident photon energy ω matches the energy differences between occupied and unoccupied atomic energy levels, the x-ray scattering amplitude from site n can be written as [24] (see the Appendix)

$$f_n(\omega) = (\hat{\epsilon}' \cdot \hat{\epsilon})f_0(\omega) - i(\hat{\epsilon}' \times \hat{\epsilon}) \cdot \widehat{\mathbf{M}}_n f_1(\omega), \quad (1)$$

where $\hat{\epsilon}$ and $\hat{\epsilon}'$ are the polarization vectors of the incident and scattering x rays, respectively, and $\widehat{\mathbf{M}}_n$ is the magnetic moment of site n . $f_0(\omega)$ is the anomalous charge scattering form factor that can be added to the Thomson scattering. $f_1(\omega)$ is the linear magnetic scattering form factor. For the experimental geometry shown in Fig. 2(a), the CD of the

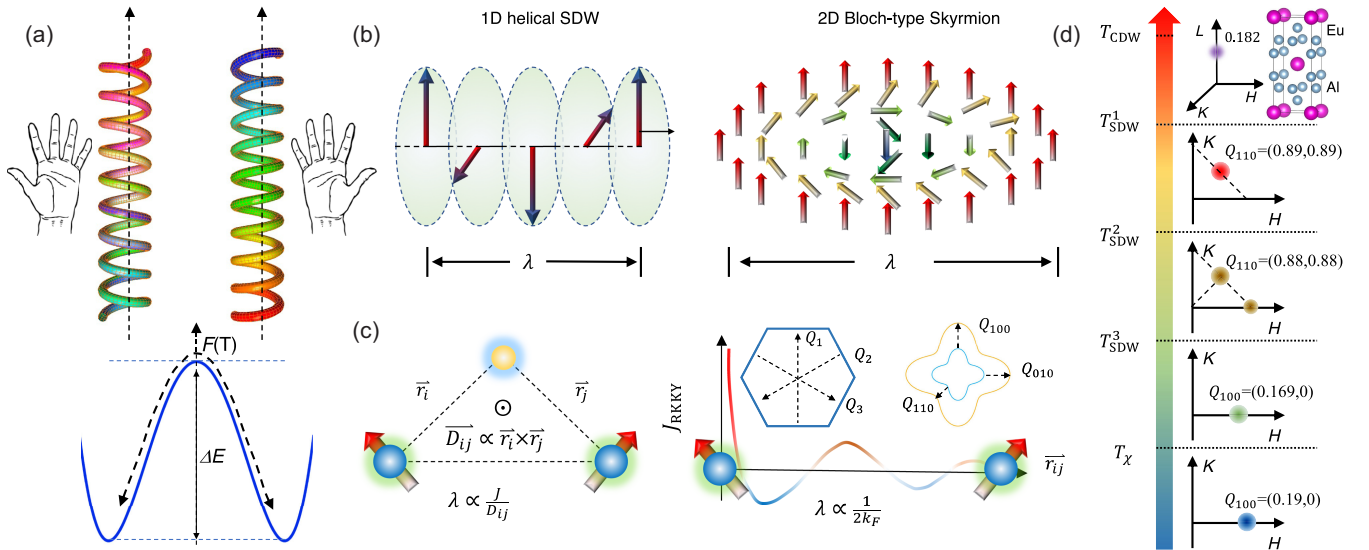


FIG. 1. Emergent chiral magnetic orders and the zero-field phase diagram of EuAl_4 . (a) Spontaneous chiral symmetry breaking yields degenerated $\chi = 1$ and $\chi = -1$ states. External field or intertwined orders can lift the degeneracy. (b) Schematics of 1D and 2D chiral spin textures, helical SDW (left) and Bloch-type skyrmion (right). (c) Possible microscopic mechanisms that drive chiral magnetic states. Left: relativistic DM interaction \mathbf{D} in noncentrosymmetric lattice determines the sign of χ (see Supplemental Material Note 1 [19]). The wavelength of the spin order λ is proportional to the relative energy scales of atomic exchange energy J and D . Right: quasi-nested Fermi surface in hexagonal and tetragonal structures give rise to frustrated RKKY interactions along $\mathbf{Q}_1, \mathbf{Q}_2, \mathbf{Q}_3$ that satisfy $\mathbf{Q}_1 + \mathbf{Q}_2 + \mathbf{Q}_3 = 0$. The inset depicts possible Fermi surface topologies in the hexagonal and tetragonal lattices that can yield nearly degenerated $\mathbf{Q}_1, \mathbf{Q}_2, \mathbf{Q}_3$ orders with $\mathbf{Q}_1 + \mathbf{Q}_2 + \mathbf{Q}_3 = 0$. The Fermi surface topology of EuAl_4 is similar to the schematic Fermi surface in the tetragonal lattice, where yellow and cyan represent electron and hole band, respectively (Supplemental Material Fig. S4). (d) Phase diagram of EuAl_4 without external magnetic field. Orthogonal CDW and SDW superlattice peaks are marked in the 3D and 2D Brillouin zone, respectively. Chiral SDW emerges below T_{SDW}^3 and breaks the C_4 rotational symmetry.

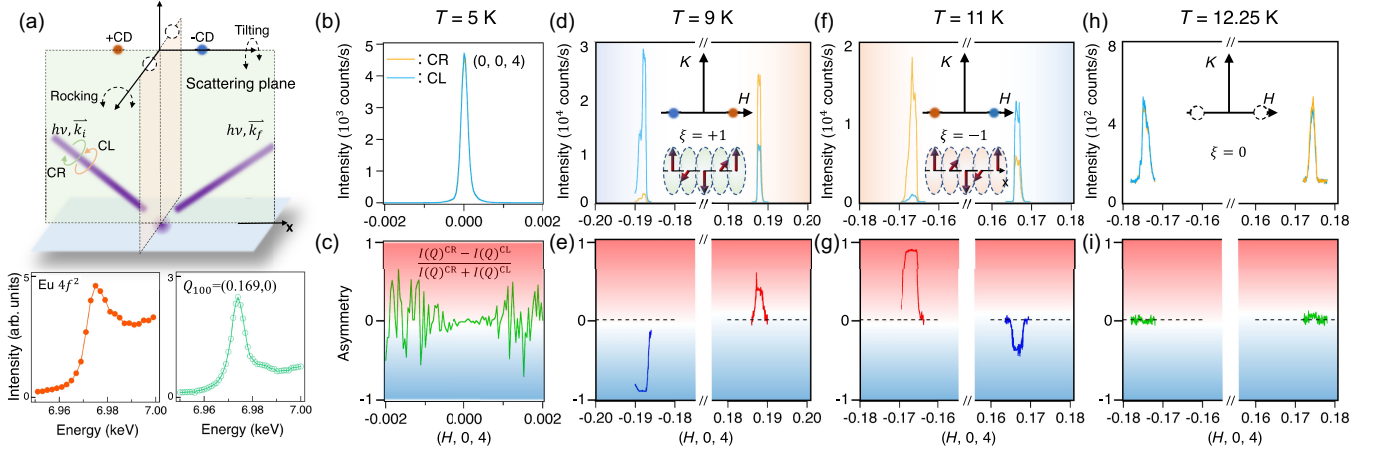


FIG. 2. Discovery of spontaneous chirality flipping in EuAl_4 . (a) Experimental geometry of CD XRDs. The photon energy was tuned to $\text{Eu } L_3$ edge to probe the magnet order parameter. For a 1D chiral SDW, the CD is given by Eq. (2), where the sign of $F(Q)$ changes from $\mathbf{Q} = \mathbf{Q}_{\text{SDW}}$ to $\mathbf{Q} = -\mathbf{Q}_{\text{SDW}}$ in the rocking scattering geometry. Here we define $\chi = +1$ if $F(\mathbf{Q}_{\text{SDW}}) > 0$. Fluorescence scan (bottom left) at $T = 5$ K shows single peak at $\omega_{\text{res}} = 6.977$ keV, confirming Eu^{2+} configuration. Magnetic resonance scan (bottom right) at $\mathbf{Q}_{\text{SDW}} = (0.169, 0, 4)$. The strong resonant enhancement confirms its magnetic origin. (b)–(i) CD of the structural and magnetic Bragg peaks. Yellow and cyan curves in (b), (d), (f), and (h) represent CR and CL incident photon polarization, respectively. Red, green, and blue curves in (c), (e), (g), and (i) represent positive, zero, and negative $F(Q)$. We note that due to the finite H component and narrow width of magnetic peaks, horizontal axis from $H = -0.17$ to 0.17 was not shown in (e), (g), and (i). Giant CD is observed below $T_{\text{SDW}}^{(3)} = 12.3$ K. The sign change of the CD shown in (e) and (g) establishes the chirality flipping across T_χ .

helical SDW can be formulated as [28]

$$I(Q)^{\text{CR}} - I(Q)^{\text{CL}} = (\tau\chi)\mathcal{D}^{yz}, \quad (2)$$

where $\tau = \text{sgn}[(\mathbf{Q}_{\text{SDW}} \cdot \vec{x})/|\mathbf{Q}_{\text{SDW}} \cdot \vec{x}|]$, \vec{x} is the unit vector along the x direction as shown in Fig. 2(a). \mathcal{D}^{yz} is a function of magnetic moment in the $(y-z)$ plane [Fig. 2(a)] and is independent of τ and χ . $I(Q)^{\text{CR}}$ and $I(Q)^{\text{CL}}$ represent x-ray intensity obtained under circular right (CR) and circular left (CL) incident photon energy, respectively. Following Eq. (2), the CD of the $\chi = 1$ helical SDW [Fig. 1(b)] is positive for a propagation vector \mathbf{Q}_{SDW} and negative for $-\mathbf{Q}_{\text{SDW}}$. An achiral SDW, such as the double- \mathbf{Q} SDW above $T_{\text{SDW}}^{(3)}$ will, therefore, yield zero CD. To probe the magnetic chirality of EuAl_4 , the photon energy is tuned to the $\text{Eu } L_3$ edge ($2p-5d$). Figure 2(a) shows the x-ray fluorescence scan at $T = 5$ K. The single peak at $\omega_{\text{res}} = 6.977$ keV confirms the Eu^{2+} electronic configuration in EuAl_4 [21]. The energy scan at fixed $\mathbf{Q}_{\text{SDW}} = (0.19, 0, 4)$ at 5 K show giant magnetic resonance at ω_{res} , confirming its magnetic origin.

In Figs. 2(b) and 2(c), we first show the CD of a structural Bragg peak $(0, 0, 4)$ at $T = 5$ K. Yellow and cyan curves represent $I(Q)^{\text{CR}}$ and $I(Q)^{\text{CL}}$, respectively. The asymmetry of the CD, $F(Q) = I(Q)^{\text{CR}} - I(Q)^{\text{CL}} / I(Q)^{\text{CR}} + I(Q)^{\text{CL}}$, is shown in Fig. 2(c). As expected, the $(0, 0, 4)$ structural Bragg peak shows $F(Q) = 0$. Note the large noise away from the Bragg condition is due to the nearly zero scattering intensity, proving the high sample quality. We then move to the helical SDW at $T = 9$ K $< T_\chi$. As shown in Figs. 2(d) and 2(e),

we observe giant CD at both \mathbf{Q}_{SDW} and $-\mathbf{Q}_{\text{SDW}}$ with $F(\mathbf{Q}_{\text{SDW}}) = 40\%$ and $F(-\mathbf{Q}_{\text{SDW}}) = -90\%$. This observation proves that the helical SDW below T_χ is chiral with $\chi = 1$. The large F indicates that the entire photon illuminated SDW (on the order of $50 \times 50 \mu\text{m}^2$) has the same χ and hence macroscopically breaks the symmetric chiral distribution. We then move to $T_\chi < T = 11$ K $< T_{\text{SDW}}^{(3)}$. Remarkably, as shown in Figs. 2(f) and 2(g), the CD changes sign with $F(\mathbf{Q}_{\text{SDW}}) = -40\%$ and $F(-\mathbf{Q}_{\text{SDW}}) = 90\%$. This observation establishes a spontaneous chirality flipping from $\chi = 1$ to $\chi = -1$. The comparably large $F(Q)$ below and above $T_{\text{SDW}}^{(4)}$ further suggests that the chirality flipping is also realized on a macroscopic length scale. The chiral density is back to nearly zero upon warming up above $T_{\text{SDW}}^{(3)}$. The giant asymmetric chiral distribution and spontaneous chirality flipping between the helical SDW states constitute the main experimental results of this work.

The spontaneous chirality flipping raises questions concerning its microscopic origin. Because of the coexistence of CDW and SDW, we first determine the complex spin-charge correlations by tracing the temperature-dependent evolution of CDW and SDW wave vectors below 20 K. The scanning trajectories in the reciprocal space are shown in the inset of Figs. 3(a)–3(c). Figure 3(d) summarizes the extracted \mathbf{Q}_{DW} (in r.l.u.). As shown in Fig. 3(a), the double- \mathbf{Q} SDW first emerges below $T_{\text{SDW}}^{(1)}$ along the $[110]$ and $[1-10]$ directions and is smoothly connected with the spin canted double- \mathbf{Q} phase. In the chiral SDW phase below $T_{\text{SDW}}^{(3)}$, \mathbf{Q}_{SDW} increases monotonically along the

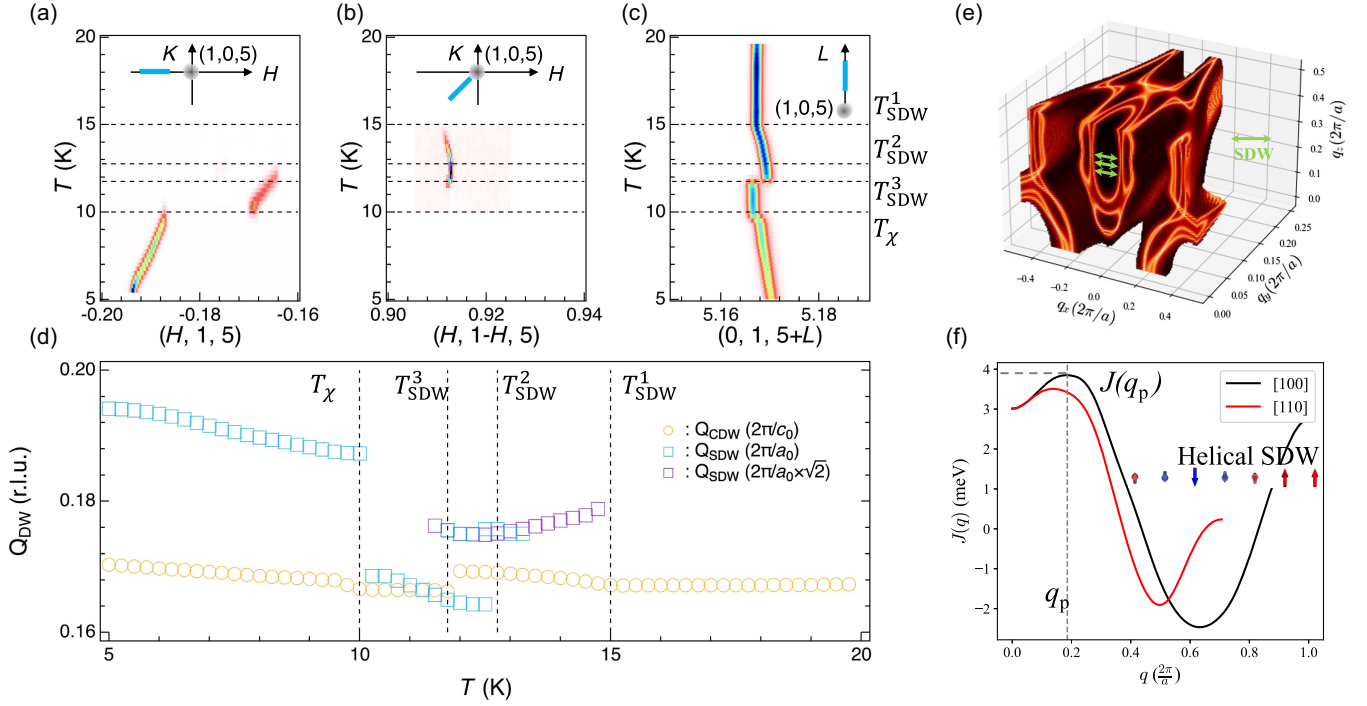


FIG. 3. Intertwined SDW and CDW with orthogonal wave vectors. (a),(b) T -dependent H scan and HK scan near the SDW wave vectors. (c) T -dependent L scan near the CDW wave vector. The scanning trajectories are shown in each panel. Dashed lines indicate the magnetic transition temperatures. (d) Extracted T -dependent CDW and SDW wave vectors. Blue and purple squares are corresponding to $|\mathbf{Q}_{\text{SDW}}|$ in the unit of $2\pi/a_0$ and $(2\pi/a_0)\sqrt{2}$, respectively. In the spin canted double- \mathbf{Q} phase between $T_{\text{SDW}}^{(2)}$ and $T_{\text{SDW}}^{(3)}$, the c -axis spin component yields superlattice peaks along $[100]$ and $[010]$ directions whose values are $\sqrt{2}$ times of the principal peak values along $[1-10]$ and $[110]$ directions. Yellow circles represent $|\mathbf{Q}_{\text{CDW}}|$ in the unit of $2\pi/c_0$. a_0 and c_0 are lattice constants in the tetragonal unit cell. (e) DFT calculated electronic structure in the tetragonal phase. Green arrows indicate the in-plane “nesting vector” that favors helical SDW. (f) Calculated RKKY interactions along $[100]$ (black line) and $[110]$ (red line) directions. The prominent peak at $q_p = 0.19$ r.l.u. is consistent with experimentally observed SDW at 5 K.

$[100]$ and $[010]$ direction and displays a discontinuous leap at the chirality flipping transition. For the CDW, the \mathbf{Q}_{CDW} first shows a rare commensurate-incommensurate transition in the temperature range $[T_{\text{SDW}}^{(3)}, 20 \text{ K}] \ll T_{\text{CDW}}$. The \mathbf{Q}_{CDW} then jumps back to the commensurate value and remains T independent in the $\chi = -1$ SDW phase ($[T_\chi, T_{\text{SDW}}^{(3)}]$). Finally, in the $\chi = 1$ SDW phase ($T < T_\chi$), the \mathbf{Q}_{CDW} once again becomes incommensurate. This complex temperature-dependent evolution of the CDW and the SDW is characteristic of intertwined spin, charge, and lattice degrees of freedom.

The incommensurability of both \mathbf{Q}_{SDW} and \mathbf{Q}_{CDW} and the presence of large itinerant carriers in EuAl_4 indicate a Fermi surface effect. Figures 3(e) and 3(f) show the calculated 3D Fermi surface and Eu-Eu magnetic interaction $J(\mathbf{q})$ of EuAl_4 in the tetragonal phase (see Supplemental Material Fig. S2 for the electronic structure determined by angle-resolved photoemission spectroscopy [19]). The highest value of $J(\mathbf{q})$ determines the Néel temperature and the wave vector \mathbf{q}_p of the helical SDW state. As shown in Fig. 3(f), $J(\mathbf{q}_p)$ along the $[100]$ direction features a typical paramagnetic spin susceptibility of a

metal with a sharp and significant finite- q peak at $q_p = 0.19$ r.l.u., consistent with experimental data at 5 K. The estimated magnetic transition temperature, $T_{\text{SDW}}^{\text{cal}} \propto J(\mathbf{q}_p)/3k_B \sim 14.8 \text{ K}$ (k_B being the Boltzmann constant), is also in agreement with experimental observation [see Supplemental Material Figs. S3–S6 for the effects of Coulomb interactions, electron temperature and magnetoelastic coupling on $J(\mathbf{q})$]. These findings provide strong numerical evidence for a Fermi surface driven helical SDW in EuAl_4 . Interestingly, the \mathbf{Q}_{CDW} matches the calculated charge susceptibility peak along the Γ - Z direction [29]. Although the primary driving force of the CDW in EuAl_4 remains to be determined, the presence of nested Fermi surface is usually helpful to select the \mathbf{Q}_{CDW} by forming a CDW gap near the Fermi level [30,31].

While the intertwined spin, charge, and lattice degrees of freedom are established in EuAl_4 , the microscopic origin of the giant asymmetric chiral distribution and spontaneous chirality flipping calls for further studies. The CD of the SDW is robust under temperature cycling above both the achiral double- \mathbf{Q} phase and $C4$ symmetry breaking (see Supplemental Material Figs. S7 and S8 [19]), suggesting

hidden chiral interactions above 20 K. Because of the intertwined nature of SDW and CDW, it is tempting to associate the chiral interaction with a chiral CDW. Encouragingly, the CDW in EuAl_4 is found to be transverse [32], where the CDW driven lattice distortions and soft phonon modes are perpendicular to the CDW propagation vector [29]. Assuming a linear transverse CDW along the propagation direction, the C_4 rotational symmetry is expected to be broken below T_{CDW} . However, the C_4 symmetry breaking in the ab plane is observed only at $T_{\text{SDW}}^{(3)} = 12.3 \text{ K} \ll T_{\text{CDW}} = 140 \text{ K}$ [20,21]. These observations, therefore, support a chiral CDW in EuAl_4 . It is highly interesting to point out that the CDW related “nesting” vector connects the topological semi-Dirac bands [33]. Similar type of band structure has been studied in 3D-quantum Hall systems, where electron-electron scattering between the Dirac bands involves chiral lattice excitations [34,35]. The role of chiral phonons in EuAl_4 is therefore an interesting open question.

Finally, we discuss the origin of chirality flipping. Since chirality is a discontinuous physical quantity, the chirality flipping requires a first-order phase transition that is consistent with the jump of \mathcal{Q}_{SDW} at T_χ . The absence of hysteresis observed in this study and previous works [20,21] suggests that the transition is weak first order [31,36]. Since the itinerant electrons play a pivotal role for both CDW and SDW in EuAl_4 , the chiral magnetic interaction is also likely momentum dependent (see Supplemental Material Notes 1 and 2 for a simplified model [19]). Depending on \mathcal{Q} , the chiral interaction energetically favors $\chi = 1$ or -1 SDW. Indeed, as we show in Figs. 3(a) and 3(d), we observe a significant jump of \mathcal{Q}_{SDW} at T_χ with minor lattice and CDW modifications.

In summary, we discovered a spontaneous chirality flipping in an orthogonal spin-charge ordered itinerant magnet. Our results highlight EuAl_4 and associated materials as a rare platform for emergent chiral interactions and open a new avenue for chiral manipulations through intertwined orders.

We thank Matthew Brahlek, Miao-Fang Chi, Xi Dai, Satoshi Okamoto, Andrew May, Brian Sales, Jiaqiang Yan, and Gabriel Kotliar for stimulating discussions. This research was supported by the U.S. Department of Energy, Office of Science, Basic Energy Sciences, Materials Sciences and Engineering Division (x-ray and ARPES measurement). CD XRMS used resources (beam line 4ID) of the Advanced Photon Source, a U.S. DOE Office of Science User Facility operated for the DOE Office of Science by Argonne National Laboratory under Contract No. DE-AC02-06CH11357. ARPES and XRMS measurements used resources at 21-ID-1 and 4-ID beam lines of the National Synchrotron Light Source II, a U.S. Department of Energy Office of Science User Facility operated for the DOE Office of Science by Brookhaven National Laboratory under Contract No. DE-SC0012704. W. R. M. acknowledges support from the Gordon and Betty Moore Foundation’s EPiQS Initiative, Grant GBMF9069 to

D.M. Y.Z. is partly supported by the National Science Foundation Materials Research Science and Engineering Center program through the UT Knoxville Center for Advanced Materials and Manufacturing (Grant No. DMR-2309083). J. B. and S. B. acknowledge financial support from the European Research Council (ERC) under the European Union’s Horizon 2020 research and innovation program (Grant No. 856538, project “3D MAGiC”) and computing time granted by the JARA-CSD and VSR Resource Allocation Board provided on the supercomputers CLAIX at RWTH Aachen University and JURECA at Juelich Supercomputer Centre under Grants No jara0219 and No jiff13. S. B. acknowledges financial support from Deutsche Forschungsgemeinschaft (DFG) through CRC 1238 (Project No. C01) and SPP 2137 (Project No. BL 444/16-2).

APPENDIX: METHODS

1. Sample growth

EuAl_4 crystals were grown from a high-temperature aluminum-rich melt [21,33]. Eu pieces (Ames Laboratory, Materials Preparation Center 99.99 + %) and Al shot (Alfa Aesar 99.999%) totaling 2.5 g were loaded into one side of a 2-mL alumina Canfield crucible set. The crucible set was sealed under 1/3 atm argon in a fused silica ampoule.

The ampoule assembly was placed in a box furnace and heated to 900 °C over 6 h (150 °C/h) and held for 12 h to melt and homogenize the metals. Crystals were precipitated from the melt during a slow cool to 700 °C over 100 h (−2 °C/h). To liberate the crystals from the remaining liquid, the hot ampoule was removed from the furnace, inverted into a centrifuge, and spun.

2. XRMS

Resonant magnetic x-ray scattering measurements were performed at the integrated *in situ* and resonant hard x-ray studies (4-ID) beam line of National Synchrotron Light Source II (NSLS-II). The photon energy, which is selected by a cryogenically cooled Si(111) double-crystal monochromator, is 6.977 keV. The sample is mounted in a closed-cycle displacive cryostat in a vertical scattering geometry, and the magnetic σ - π scattering channel is measured using an Al(222) polarization analyzer and silicon drift detector.

3. CD XRMS

The CD XRMS were performed at the 4-ID-D beam line of the Advanced Photon Source (APS), Argonne National Laboratory (ANL). The photon energy was tuned to the Eu L_3 resonance (6.977 keV) using a double-crystal Si (111) monochromator. Circularly polarized x rays were generated using a 180- μm -thick diamond (111) phase plate [34], focused to $200 \times 100 \mu\text{m}^2$ full width at half maximum (FWHM) using a toroidal mirror, and further reduced to $50 \times 50 \mu\text{m}^2$ FWHM with slits. Temperature

was controlled using a He closed-cycle cryostat. Diffraction was measured in reflection from the sample [001] surface using vertical scattering geometry and an energy dispersive silicon drift detector (approximately 0.15 keV energy resolution).

4. Angle-resolved photoemission spectroscopy (ARPES)

The angle-resolved photoemission spectroscopy (ARPES) experiments were performed on single crystals EuAl_4 . The samples were cleaved *in situ* in a vacuum better than 3×10^{-11} torr. The experiment was performed at beam line 21-ID-1 at the NSLS-II. The measurements were taken with synchrotron light source and a Scienta-Omicron DA30 electron analyzer. The total energy resolution of the ARPES measurement is approximately 15 meV. The sample stage is maintained at $T = 20$ K throughout the experiment.

5. Density functional theory (DFT)

The first-principles simulations are performed using the all-electron full-potential Korringa-Kohn-Rostoker (KKR) Green function method [37] in the scalar relativistic approximation. The inclusion of the spin-orbit coupling self-consistently does not alter the magnetic interactions or Fermi surface. The Eu^{2+} and its $4f$ electrons are treated using the DFT + U approach [38] with value of $U = 2$ eV. The calculations are carried out using an angular momentum cutoff of $l_{\text{max}} = 4$ in the orbital expansion of the Green function. Accurate self-consistent results were obtained using 58 integration points along the complex energy contour and a $30 \times 30 \times 30$ k mesh for the Brillouin zone integration. The magnetic interactions between the Eu magnetic atoms are computed in real space using the infinitesimal rotation method [39]. These interactions are then Fourier transformed into reciprocal space with a cutoff of 10 lattice constants to accurately account for the long-range RKKY interactions. The Fermi surface is imaged by computing q -dependent density of states [40].

6. XRMS cross section

Under the electric dipole approximation, the resonant scattering process involves transitions between the core state $|\zeta_v\rangle$ with energy E_v and an unoccupied state $|\psi_\eta\rangle$ with energy E_η in both absorption and emission channel. The scattering amplitude can be written as

$$f_{\text{res}}(\omega) = \sum_{ij} \hat{\epsilon}'_i \hat{\epsilon}_j \sum_{\eta} \frac{\langle \zeta_v | R_i | \psi_\eta \rangle \langle \psi_\eta | R_j | \zeta_v \rangle}{\omega - (E_\eta - E_v) + i\Gamma} = \sum_{ij} \hat{\epsilon}'_i \hat{\epsilon}_j T_{ij}, \quad (\text{A1})$$

where $\hat{\epsilon}$ and $\hat{\epsilon}'$ are the polarization vectors of the incident and scattering x rays, respectively. R is the position operator. When the resonant atom has a parity-even

magnetic moment \widehat{M}_n at site n , and assuming cylindrical symmetry, the magnetic scattering takes the form [24]:

$$f_n(\omega) = (\hat{\epsilon}' \cdot \hat{\epsilon}) f_0(\omega) - i(\hat{\epsilon}' \times \hat{\epsilon}) \times \widehat{M}_n f_1(\omega) + (\hat{\epsilon}' \cdot \widehat{M}_n)(\hat{\epsilon} \cdot \widehat{M}_n) f_2(\omega). \quad (\text{A2})$$

Since $f_2(\omega)$ is usually much smaller than $f_1(\omega)$, the magnetic scattering is dominated by the second term of Eq. (A2). For the 1D helical SDW, the CD has been derived, respectively, for the tilting and rocking geometries shown in Fig. 2(a) [28]. For the chiral Bloch-type SDW,

$$I(Q)^{\text{CR}} - I(Q)^{\text{CL}} = (\tau\chi)\mathcal{D}^{yz} \text{ in the rocking geometry.} \quad (\text{A3})$$

For the achiral Néel-type SDW,

$$I(Q)^{\text{CR}} - I(Q)^{\text{CL}} = \chi\mathcal{B}^{yz} \text{ in the tilting geometry.} \quad (\text{A4})$$

Note that for the Néel-type SDW, the CD does not change sign from the positive to negative propagation vector. Our experiment was performed in the rocking geometry that shows sign change for the chiral Bloch-type SDW.

7. Nonresonant XRMS cross section

For nonresonant scattering, the x-ray scattering amplitude can be written as

$$f_{\text{non}}(\omega) \propto \sum_j \langle 0 | e^{i\vec{q} \cdot \vec{r}_j} | \rangle (\vec{\epsilon}'^* \cdot \vec{\epsilon}) - i \frac{\hbar\omega}{mc^2} \left[\frac{mc}{e\hbar} \langle 0 | \hat{q} \times [\vec{M}_L(\vec{q}) \times \hat{q}] | 0 \rangle \cdot \vec{P}_L + \frac{mc}{e\hbar} \langle 0 | [\vec{M}_S(\vec{q})] | 0 \rangle \cdot \vec{P}_S \right], \quad (\text{A5})$$

where \vec{M}_L and \vec{M}_S are Fourier transform of orbital and spin moment density, respectively. Here,

$$\vec{P}_L = 4 \sin^2\theta (\vec{\epsilon}'^* \times \vec{\epsilon}), \quad (\text{A6})$$

$$\vec{P}_S = \vec{\epsilon} \times \vec{\epsilon}' + (\hat{k}_f \times \vec{\epsilon}'^*)(\hat{k}_f \cdot \vec{\epsilon}) - (\hat{k}_i \times \vec{\epsilon})(\hat{k}_i \cdot \vec{\epsilon}'^*) - (\hat{k}_f \times \vec{\epsilon}'^*) \times (\hat{k}_i \times \vec{\epsilon}). \quad (\text{A7})$$

Equations (A5)–(A7) show that the nonresonant x-ray scattering can also probe spin and orbital magnetic moment and display CD. However, the factor $\hbar\omega/mc^2$ in Eq. (A5) at $\hbar\omega \sim 10$ keV is on the order of $\sim 10^{-4}$. Therefore, for the nonresonant x-ray scattering, the cross section related to Eqs. (A6) and (A7) is extremely small, typically 10–30 counts/s for magnetic materials.

In our study, we observed both CD and asymmetry of the CD that is described in Eq. (A4). Furthermore, $F(Q) = I(Q)^{\text{CR}} - I(Q)^{\text{CL}} / I(Q)^{\text{CR}} + I(Q)^{\text{CL}} \sim 90\%$ is very large, excluding contributions from Eqs. (A6) and (A7) as the origin of chirality flipping.

-
- [1] F. D. M. Haldane, *Model for a quantum Hall effect without Landau levels: Condensed-matter realization of the parity anomaly*, *Phys. Rev. Lett.* **61**, 2015 (1988).
- [2] X. G. Wen, F. Wilczek, and A. Zee, *Chiral spin states and superconductivity*, *Phys. Rev. B* **39**, 11413 (1989).
- [3] T. H. R. Skyrme, *A unified field theory of mesons and baryons*, *Nucl. Phys.* **31**, 556 (1962).
- [4] U. K. Rößler, N. Bogdanov, and C. Pfleiderer, *Spontaneous skyrmion ground states in magnetic metals*, *Nature (London)* **442**, 797 (2006).
- [5] Y.-X. Jiang *et al.*, *Unconventional chiral charge order in kagome superconductor KV₃Sb₅*, *Nat. Mater.* **20**, 1353 (2021).
- [6] X. Feng, K. Jiang, Z. Wang, and J. P. Hu, *Chiral flux phase in the kagome superconductor AV₃Sb₅*, *Sci. Bull.* **66**, 1384 (2021).
- [7] M. M. Denner, R. Thomaly, and T. Neupert, *Analysis of charge order in the kagome metal AV₃Sb₅ (A = K, Rb, Cs)*, *Phys. Rev. Lett.* **127**, 217601 (2021).
- [8] X. Teng *et al.*, *Discovery of charge density wave in a correlated kagome lattice antiferromagnet*, *Nature (London)* **609**, 490 (2022).
- [9] Y. Zhang, Y. Ni, H. Zhao, S. Hakani, F. Ye, L. DeLong, I. Kimchi, and G. Cao, *Control of chiral orbital currents in a colossal magnetoresistance material*, *Nature (London)* **611**, 467 (2022).
- [10] H. Chen *et al.*, *Roton pair density wave in a strong-coupling kagome superconductor*, *Nature (London)* **599**, 222 (2021).
- [11] L. Jiao, S. Howard, S. Ran, Z. Wang, J. O. Rodriguez, M. Sigrist, Z. Wang, N. P. Butch, and V. Madhavan, *Chiral superconductivity in heavy-fermion metal UTe₂*, *Nature (London)* **579**, 523 (2020).
- [12] I. M. Hayes *et al.*, *Multicomponent superconducting order parameter in UTe₂*, *Science* **373**, 797 (2021).
- [13] N. Nagaosa and Y. Tokura, *Topological properties and dynamics of magnetic skyrmions*, *Nat. Nanotechnol.* **8**, 899 (2013).
- [14] S.-W. Cheong and X. Xu, *Magnetic chirality*, *npj Quantum Mater.* **7**, 40 (2022).
- [15] Z. Wang, Y. Su, S. Z. Lin, and C. D. Batista, *Skyrmion crystal from RKKY interaction mediated by 2D electron gas*, *Phys. Rev. Lett.* **124**, 207201 (2020).
- [16] J. Bouaziz, E. Mendive-Tapia, S. Blugel, and J. B. Staunton, *Fermi-surface origin of skyrmion lattices in centrosymmetric rare-earth intermetallics*, *Phys. Rev. Lett.* **128**, 157206 (2022).
- [17] N. Ghimire *et al.*, *Competing magnetic phases and fluctuation-driven scalar spin chirality in the kagome metal YMn₆Sn₆*, *Sci. Adv.* **6**, eabe2680 (2020).
- [18] S.-Y. Xu *et al.*, *Spontaneous gyrotropic electronic order in a transition-metal dichalcogenide*, *Nature (London)* **578**, 545 (2020).
- [19] See Supplemental Material at <http://link.aps.org/supplemental/10.1103/PhysRevX.14.011053> for additional x-ray and ARPES data, DFT calculations, and model analysis.
- [20] R. Takagi *et al.*, *Square and rhombic lattices of magnetic skyrmions in a centrosymmetric binary compound*, *Nat. Commun.* **13**, 1472 (2022).
- [21] W. R. Meier, J. R. Torres, R. P. Hermann, J. Zhao, B. Lavina, B. C. Sales, and A. F. May, *Thermodynamic insights into the intricate magnetic phase diagram of EuAl₄*, *Phys. Rev. B* **106**, 094421 (2022).
- [22] T. Shang, Y. Xu, D. J. Gawryluk, J. Z. Ma, T. Shiroka, M. Shi, and E. Pomjakushina, *Anomalous Hall resistivity and possible topological Hall effect in the EuAl₄ antiferromagnet*, *Phys. Rev. B* **103**, L020405 (2021).
- [23] P. Lee, T. Rice, and P. Anderson, *Conductivity from charge or spin density waves*, *Solid State Commun.* **14**, 703 (1974).
- [24] J. P. Hannon, G. T. Trammell, M. Blume, and D. Gibbs, *X-ray resonance exchange scattering*, *Phys. Rev. Lett.* **61**, 1245 (1988).
- [25] H. A. Dürr, E. Dudzik, S. S. Dhesi, J. B. Goedkoop, G. van der Laan, M. Belakhovsky, C. Mocuta, A. Marty, and Y. Samson, *Chiral magnetic domain structures in ultrathin FePd films*, *Science* **284**, 2166 (1999).
- [26] S. L. Zhang, G. van der Laan, and T. Hesjedal, *Direct experimental determination of the topological winding number of skyrmions in Cu₂OSeO₃*, *Nat. Commun.* **8**, 14619 (2017).
- [27] J.-Y. Chauléau, W. Legrand, N. Reyren, D. Maccariello, S. Collin, H. Popescu, K. Bouzehouane, V. Cros, N. Jaouen, and A. Fert, *Chirality in magnetic multilayers probed by the symmetry and the amplitude of dichroism in x-ray resonant magnetic scattering*, *Phys. Rev. Lett.* **120**, 037202 (2018).
- [28] K. T. Kim, J. Y. Kee, M. R. McCarter, G. van der Laan, V. A. Stoica, J. W. Freeland, R. Ramesh, S. Y. Park, and D. R. Lee, *Origin of circular dichroism in resonant elastic x-ray scattering from magnetic and polar chiral structure*, *Phys. Rev. B* **106**, 035116 (2022).
- [29] L. L. Wang, N. K. Nepal, and P. C. Canfield, *Origin of charge density wave in topological semimetals SrAl₄ and EuAl₄*, [arXiv:2306.15068](https://arxiv.org/abs/2306.15068).
- [30] H. Miao, D. Ishikawa, R. Heid, M. Le Tacon, G. Fabbris, D. Meyers, G. D. Gu, A. Q. R. Baron, and M. P. M. Dean, *Incommensurate phonon anomaly and the nature of charge density waves in cuprates*, *Phys. Rev. X* **8**, 011008 (2018).
- [31] H. Miao *et al.*, *Signature of spin-phonon coupling driven charge density wave in a kagome magnet*, *Nat. Commun.* **14**, 6183 (2023).
- [32] S. Ramakrishnan *et al.*, *Orthorhombic charge density wave on the tetragonal lattice of EuAl₄*, *IUCrJ* **9**, 378 (2022).
- [33] Wang *et al.*, *Crystalline symmetry-protected non-trivial topology in prototype compound BaAl₄*, *npj Quantum Mater.* **6**, 28 (2021).
- [34] F. Tang *et al.*, *Three-dimensional quantum Hall effect and metal-insulator transition in ZrTe₅*, *Nature (London)* **569**, 537 (2019).

- [35] K. Luo and X. Dai, *Transverse Peierls transition*, *Phys. Rev. X* **13**, 011027 (2023).
- [36] H. Miao *et al.*, *Geometry of the charge density wave in the kagome metal AV₃Sb₅*, *Phys. Rev. B* **104**, 195132 (2021).
- [37] P. Rößmann *et al.*, *JuDFtteam/JuKKR: v3.6 (v3.6)*, Zenodo (2022), [10.5281/zenodo.7284739](https://doi.org/10.5281/zenodo.7284739).
- [38] S. L. Dudarev, P. Liu, D. A. Andersson, C. R. Stanek, T. Ozaki, and C. Franchini, *Parametrization of LSDA + U for noncollinear magnetic configurations*, *Phys. Rev. Mater.* **3**, 083802 (2019).
- [39] A. I. Liechtenstein, M. I. Katsnelson, and V. A. Gubanov, *Exchange interactions and spin-wave stiffness in ferromagnetic metals*, *J. Phys. F* **14**, L125 (1984).
- [40] H. Ebert, D. Ködderitzsch, and J. Minár, *Calculating condensed matter properties using the KKR-Green's function method—Recent developments and applications*, *Rep. Prog. Phys.* **74**, 096501 (2011).